PL-TR-92-2110(II)

AD-A252 442

(2)

DATA TO TEST AND EVALUATE THE PERFORMANCE OF NEURAL NETWORK ARCHITECTURES FOR SEISMIC SIGNAL DISCRIMINATION

NEURAL COMPUTING FOR SEISMIC PHASE IDENTIFICATION

Gagan B. Patnaik
Thomas J. Sereno, Jr.

Science Applications International Corporation
10260 Campus Point Drive
San Diego, California 92121

27 September 1991

Scientific Report No. 1 (Volume II)

PHILLIPS LABORATORY
AIR FORCE SYSTEMS COMMAND
HANSCOM AIR FORCE BASE, MASSACHUSETTS 01731-5000

SPONSORED BY
Defense Advanced Research Projects Agency
Nuclear Monitoring Research Office
ARPA ORDER NO. 5307

MONITORED BY
Phillips Laboratory
Contract No. F19628-90-C-0156

The views and conclusions contained in this document are those of the authors and should not be interpreted as representing the official policies, either expressed or implied, of the Defense Advanced Research Projects Agency or the U.S. Government.

This technical report has been reviewed and is approved for publication.

JAMES F. LEWKOWICZ
Contract Manager
Solid Earth Geophysics Branch
Earth Sciences Division

JAMES F. LEWKOWICZ
Branch Chief
Solid Earth Geophysics Branch
Earth Sciences Division

DONALD H. ECKHARDT, Director
Earth Sciences Division

This report has been reviewed by the ESD Public Affairs Office (PA) and is releasable to the National Technical Information Service (NTIS).

Qualified requestors may obtain additional copies from the Defense Technical Information Center. All others should apply to the National Technical Information Service.

If your address has changed, or if you wish to be removed from the mailing list, or if the addressee is no longer employed by your organization, please notify PL/IMA, Hanscom AFB, MA 01731-5000. This will assist us in maintaining a current mailing list.

Do not return copies of this report unless contractual obligations or notices on a specific document requires that it be returned.

REPORT DOCUMENTATION PAGE

Form Approved
OMB No. 0704-0188

1. AGENCY USE ONLY *(Leave blank)*

2. REPORT DATE 27 September 1991

3. REPORT TYPE AND DATES COVERED Scientific Report #1 (Volume II)

4. TITLE AND SUBTITLE Data to Test and Evaluate the Performance of Neural Architectures for Seismic Signal Discrimination. Neural Computing for Seismic Phase Identification

5. FUNDING NUMBERS
PE 61101E
PR 9T10 TA DA WU AA

Contract F19628-90-C-0156

6. AUTHOR(S)
Gagan B. Patnaik
Thomas J. Sereno, Jr

7. PERFORMING ORGANIZATION NAME(S) AND ADDRESS(ES)
Science Applications Intern'l Corp
10260 Campus Point Drive
San Diego, CA 92121

8. PERFORMING ORGANIZATION REPORT NUMBER

9. SPONSORING/MONITORING AGENCY NAME(S) AND ADDRESS(ES)
Phillips Laboratory
Hanscom AFB, MA 01731-5000

Contract Manager: James Lewkowicz/GPEH

10. SPONSORING/MONITORING AGENCY REPORT NUMBER
PL-TR-92-2110 (II)

11. SUPPLEMENTARY NOTES

12a. DISTRIBUTION/AVAILABILITY STATEMENT
Approved for public release;
Distribution unlimited

12b. DISTRIBUTION CODE

13. ABSTRACT *(Maximum 200 words)*

This report describes the application of a neural computing approach for automated initial identification of seismic phases (*P* or *S*) recorded by 3-component stations. We use a 3-layer back-propagation neural network to identify phases on the basis of their polarization attributes. This approach is much easier to develop than a more traditional rule-based system because of the high-dimensionality of the input (8-10 polarization attributes), and because the data are station-dependent. The neural network approach also performs 3-7% better than a linear multivariate method. Most of the gain is for signals with low signal-to-noise ratio since the non-linear neural network classifier is less sensitive to outliers (or noisy data) than the linear multivariate method. Another advantage of the neural network approach is that it is easily adapted to data recorded by new stations. For example, we find that we achieve 75-80% identification accuracy for a new station without system retraining (e.g., using a network derived from data from a different station). The data required for retraining can be accumulated in about two weeks of continuous operation of the new station, and training takes less than one hour on a Sun4 Sparc station. After this retraining, the identification accuracy increases to > 90%. We have recently added "context" (e.g., the number of arrivals before and after the arrival under consideration) to the input of the neural network, and we have found that this further improves the identification accuracy by 3-5%. This neural network approach performs better than competing technologies for automated initial phase identification, and it is amenable to machine-learning techniques to automate the process of acquiring new knowledge.

14. SUBJECT TERMS
Neural networks
Phase identification
Polarization
Regional seismology

15. NUMBER OF PAGES 42

16. PRICE CODE

17. SECURITY CLASSIFICATION OF REPORT	18. SECURITY CLASSIFICATION OF THIS PAGE	19. SECURITY CLASSIFICATION OF ABSTRACT	20. LIMITATION OF ABSTRACT
Unclassified	Unclassified	Unclassified	SAR

NSN 7540-01-280-5500

Standard Form 298 (Rev 2-89)
Prescribed by ANSI Std Z39-18
298-102

Table of Contents

Page

List of Figures

Tables:

1. INTRODUCTION

1.1 Objectives

The main objectives of this two-year study are described in Volume I of this annual report. The first objective is to assemble data sets to be used for test and evaluation of the performance of neural networks for automated processing and interpretation of seismic data. These data sets are provided to MIT Lincoln Laboratory for their effort on the development of neural networks for seismic application under DARPA's Artificial Neural Network Technology program.

A second objective of this study is to evaluate the results of this neural network program in the context of monitoring nuclear explosion testing. To achieve this objective, we will test and evaluate the neural network application developed by MIT Lincoln Laboratory, and we have developed our own neural network application for automated initial identification of seismic phases (*P* or *S*) using data recorded by 3-component stations.

1.2 Current Status

A major effort during the first year of this project was spent on the development of data sets for test and evaluation of neural networks for seismic signal processing and interpretation. This effort is described in detail in Volume I of the report [*Sereno and Patnaik,* 1991].

An important problem in automated seismic data interpretation is initial phase identification (*P* or *S*) using data recorded by 3-component stations. We developed and tested a neural network approach to this problem using data recorded by the 3-component elements of the array stations ARCESS, NORESS, FINESA and GERESS, and 3-component stations in Poland (KSP) and in the former Soviet Union (GARM). Since the polarization data from array stations are averaged during IMS processing, we also applied our method separately to data recorded by the individual 3-component elements of ARCESS and NORESS. The neural network results were compared to results from a linear multivariate analysis of the same data, and adaptability of the neural networks was examined by testing them with data from stations in other geological environments. We implemented our neural network software into a test version of ESAL (Expert System for Association and Location), which is a knowledge-based component of the Intelligent Monitoring System (IMS). The integration and testing of the first version of the module is complete. We will begin testing and evaluating its performance as soon as data from the IRIS stations become available. The next version of this software will accommodate "context" as input to the trained neural network, which has shown improvement in identification by 3-5%, compared to using polarization data alone.

1.3 Outline of the Report

This annual report is divided into two volumes. Volume I is a description of Data Set #1 that was provided to MIT Lincoln Laboratory for their neural network application development [*Sereno and Patnaik*, 1991]. Volume II (this report) describes the results of our neural network application to the problem of initial phase identification, using polarization attributes derived from data recorded by 3-component stations. Descriptions of the design, development and testing of the neural networks are provided. Preliminary results of comparative evaluation of the neural network approach with the multivariate discriminant analysis are also reported. Finally, this report describes of the work being done on the implementation of the developed neural network module into the IMS.

Section 2 describes the data used for neural network training and testing. Section 3 describes the neural network simulation. Section 3.1 describes why we use the neural network approach. Section 3.2 describes back propagation neural networks and the architecture used in this study. Section 3.3 describes the methods adopted for network parameter estimation, preprocessing strategy for the input parameters, and the methods of training and testing. Section 4 describes our results. Section 4.1 gives results of each 3-component element of the arrays NORESS and ARCESS. Section 4.2 describes the comparative evaluation of the results with those obtained from a multivariate discriminant analysis method. Section 4.3 describes the adaptability of the trained neural networks to other geological conditions. Section 4.4 describes the on-going work for improving the identification performance by adding context in the simulation. Section 5 describes the on-going work on the integration of our neural networks into IMS. Finally, Section 6 summarizes the study of neural computing for initial seismic phase identification.

2. THE DATA

The data used in this study are primarily the polarization parameters that are routinely computed by the IMS and written to an on-line relational database at CSS [*Bache, et. al.*, 1990]. These data are associated with regional *P*-type and *S*-type phases that have been identified by seismic analysts at NORSAR and CSS. The analysts' identifications of these phases are used as ground-truths for neural network training. We used data from four regional arrays (ARCESS, NORESS, FINESA and GERESS), and two 3-component stations (KSP and GARM). The locations of these stations are plotted in Figure 1.

LOCATION OF THE ARRAYS AND SINGLE STATIONS

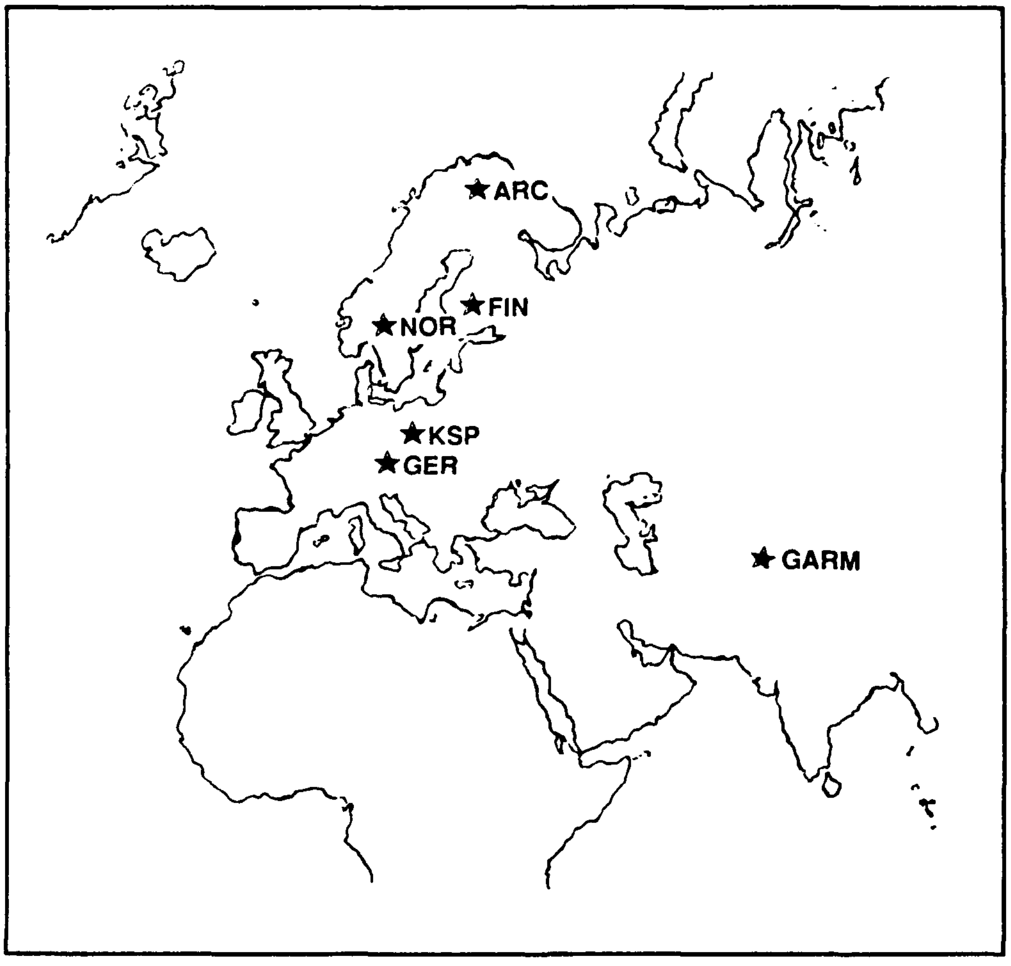

Figure 1. *The location of the high-frequency arrays ARCESS (ARC), FINESA (FIN), GERESS (GER), NORESS (NOR), and 3-component stations KSP and GARM are shown.*

The method used in IMS for particle-motion analysis was developed by *Jurkevics* [1988]. It computes a polarization ellipsoid within overlapping time windows by solving the eigenproblem of the covariance matrix. Data from the 3-component sensors from the arrays are combined by averaging the individual covariance matrices before solving the eigenproblem. The covariance matrices are computed in the time domain for several frequency bands, and then normalized and averaged to obtain a wide-band estimate for each of the overlapping windows. The IMS implementation of this is described by *Bache, et. al.*, [1990].

The effects of signal-to-noise ratio (*snr*) on the polarization parameter estimation have been studied in detail by *Suteau-Henson* [1991]. Large scatter is observed for data with *snr* < 2.0. Therefore, we have considered two separate categories of data (all *snr* and *snr* > 2.0) for all of our neural network simulations. The *snr* is the ratio of the maximum signal 3-component amplitude to the maximum pre-arrival noise 3-component amplitude. The 3-component amplitude is measured from the time window with maximum rectilinearity, and is equal to the sum of the square roots of the eigenvalues (i.e., it is the sum of the amplitudes measured along the three axes of the polarization ellipsoid).

Several of the particle motion attributes are calculated from the time window with the maximum rectilinearity. These are called *P*-type attributes in the descriptions below. Also, several attributes are calculated from the time window with maximum 3-component amplitude. They are called *S*-type attributes. The polarization attributes used in this study are defined as:

freq: Center frequency of the passbands with *snr* >1.5 used in the averaging. The passbands are 1-2, 2-4, 4-8 and 8-16 Hz. For example, if all bands had *snr* > 1.5, then *freq* would be 8.5 Hz.

rect: Signal rectilinearity defined as:

$$rect = \left[1 - \frac{(\lambda_3 + \lambda_2)}{2\lambda_1}\right]$$

where λ_1, λ_2, and λ_3 are the eigenvalues such that $\lambda_1 > \lambda_2 > \lambda_3$. *rect* is a *P*-type attribute.

plans: Signal planarity defined as:

$$plans = 1 - \frac{\lambda_3}{\lambda_2}$$

Planarity is measured from the window with the maximum 3-component amplitude (*S*-type attribute).

hvrat: Horizontal to vertical power ratio defined as:

$$hvrat = \frac{c_3 + c_2}{2c_1}$$

where c_1, c_2, and c_3 are the diagonal elements of the covariance matrix, and c_1 corresponds to the vertical component. *hvrat* is an *S*-type attribute.

hvratp: Similar to *hvrat*, but measured at the time of maximum rectilinearity. It is a *P*-type attribute.

hmxmn: Maximum to minimum horizontal amplitude ratio defined as:

$$hmxmn = \sqrt{\frac{\lambda_1}{\lambda_2}}$$

where λ_1 and λ_2 are the maximum and minimum eigenvalues obtained by solving the 2-D eigensystem, using only the horizontal components. It is an *S*-type attribute.

inang3: Incidence angle (measured from the vertical) of the eigenvector associated with the smallest eigenvalue. It is also called the short-axis incidence angle and is an *S*-type attribute.

inang1: Apparent incidence angle (measured from the vertical) of the eigenvector associated with the largest eigenvalue. It is also called the long-axis incidence angle, or the emergence angle and is a *P*-type attribute.

Figures 2 - 9 show histograms of these attributes for *P*-type and *S*-type phases recorded by each of the stations mentioned previously. The number of *P*-type and *S*-type phases that are used for each station are shown in parentheses and range from a few hundred to several thousand. In addition to noticeable station-dependence in these data, (e.g., *P*-rectilinearity at NORESS), these histograms show considerable overlap for *P*-type and *S*-type phases. This is in contrast to the array measurement of phase velocity (Figure 10). Accurate estimates of this single parameter enable near perfect identification of *P*-type and *S*-type phases for array data. Since this parameter is not available for single 3-component data, automated phase identification is performed from the polarization attributes. Neural network classifiers are well-suited for this type of situation since they are capable of constructing non-linear decision surfaces across complex class boundaries from high-dimensional input data.

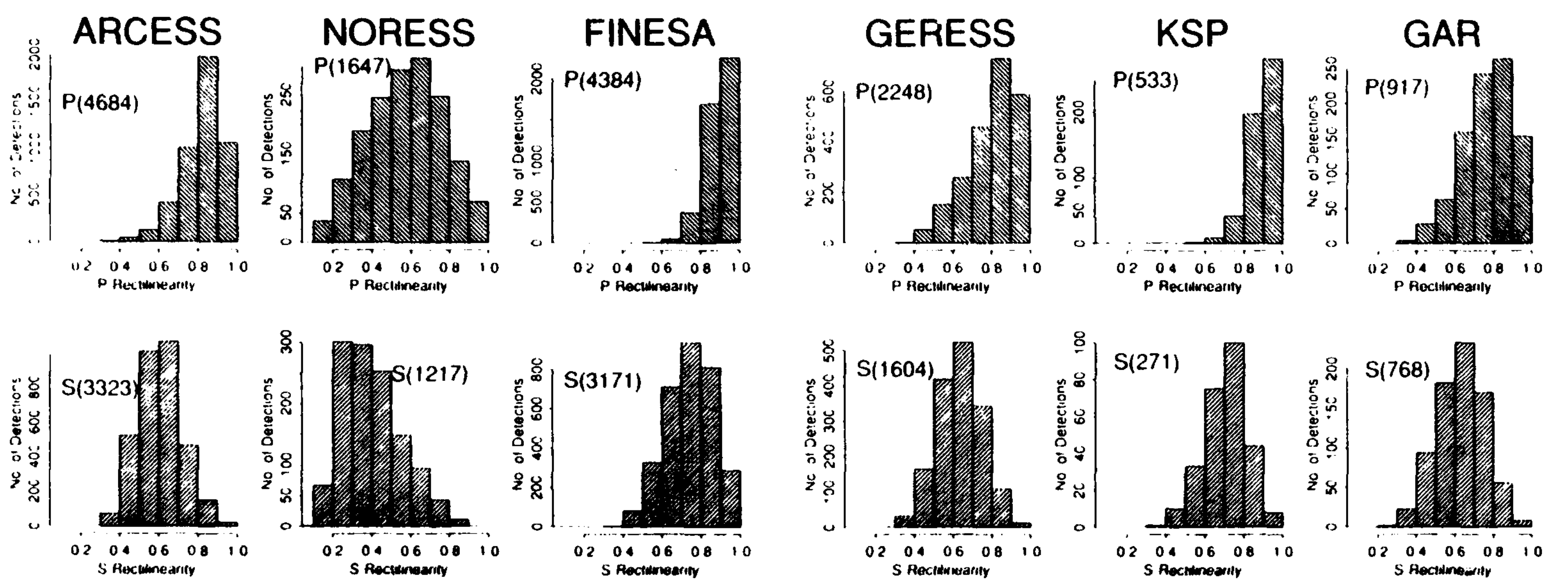

Figure 2. *Histograms of "rectilinearity" are shown for P-type phases (upper) and S-type phases (lower). The numbers in parentheses indicate the number of associated phases. The P and S populations show overlaps at all observing stations.*

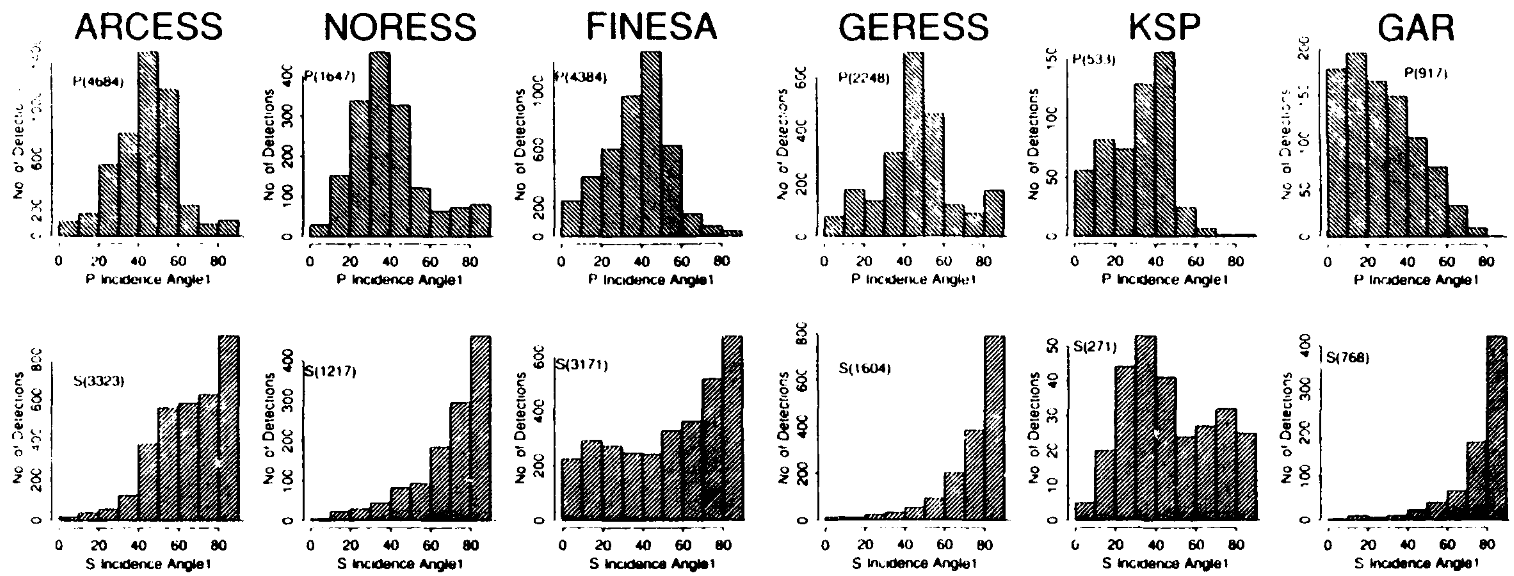

Figure 3. *Histograms of "long-axis incidence angle" are shown for P-type phases (upper) and S-type phases (lower). The numbers in parentheses indicate the number of associated phases. The P and S populations show overlaps at all observing stations.*

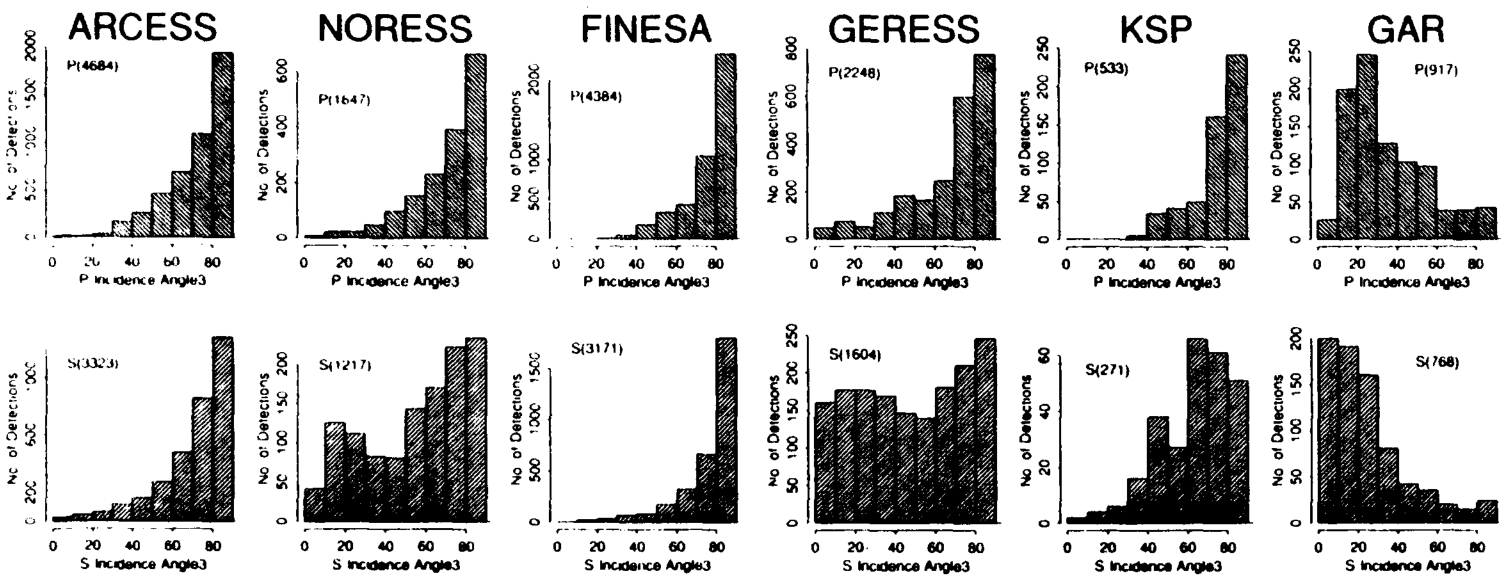

Figure 4. *Histograms of "short-axis incidence angle" are shown for P-type phases (upper) and S-type phases (lower). The numbers in parentheses indicate the number of associated phases. The P and S populations show overlaps at all observing stations.*

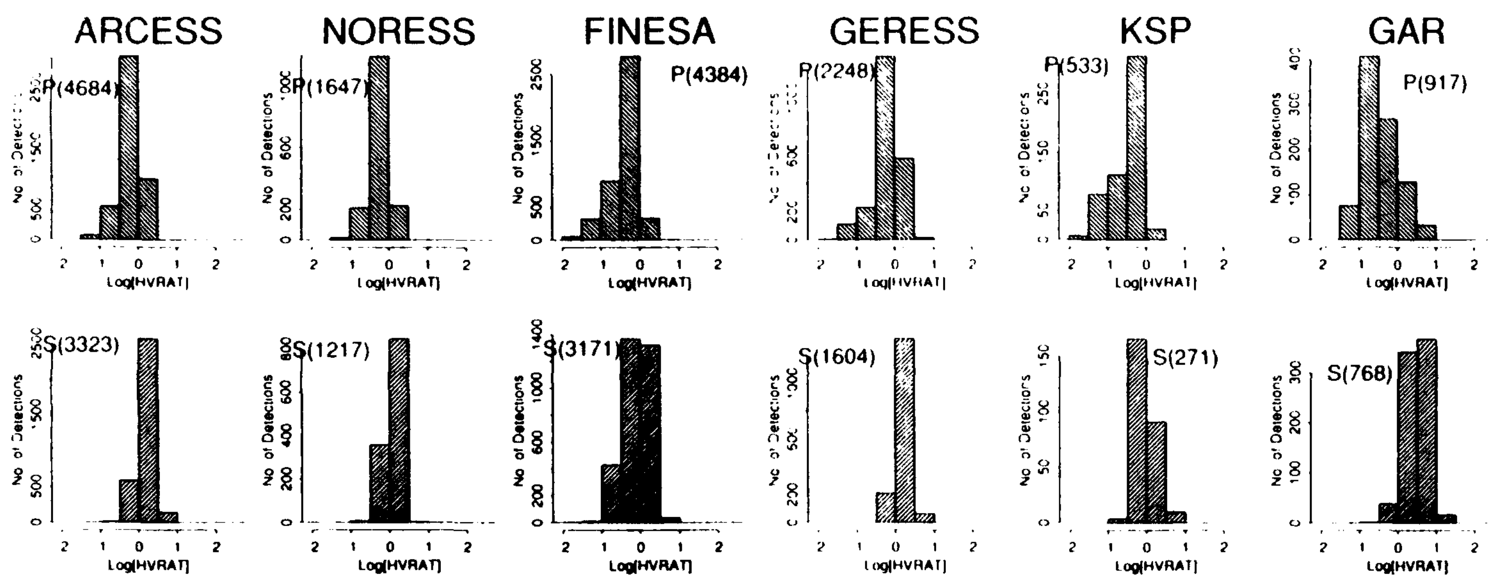

Figure 5. *Histograms of "logarithm of the ratio of horizontal to vertical power" are shown for P-type phases (upper) and S-type phases (lower). The numbers in parentheses indicate the number of associated phases. The P and S populations show overlaps at all observing stations.*

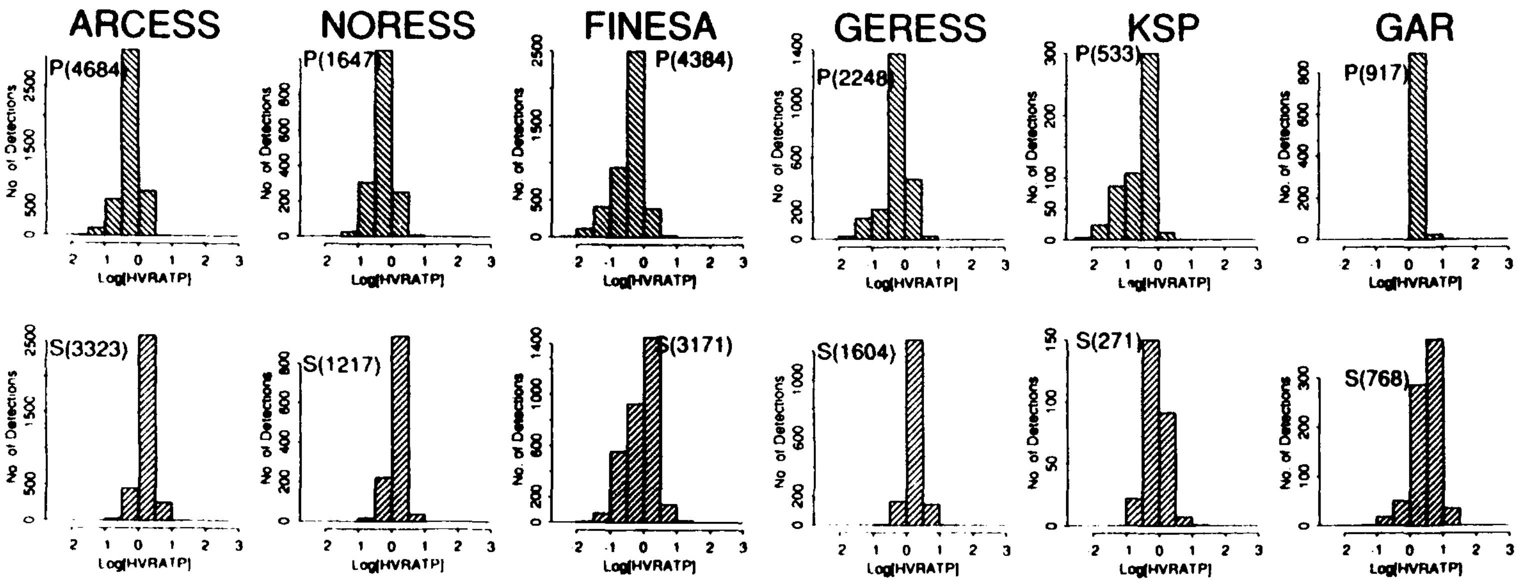

Figure 6. *Histograms of "logarithm of the ratio of horizontal to vertical power at the time of maximum rectilinearity" are shown for P-type phases (upper) and S-type phases (lower). The numbers in parentheses indicate the number of associated phases. The P and S populations show overlaps at all observing stations.*

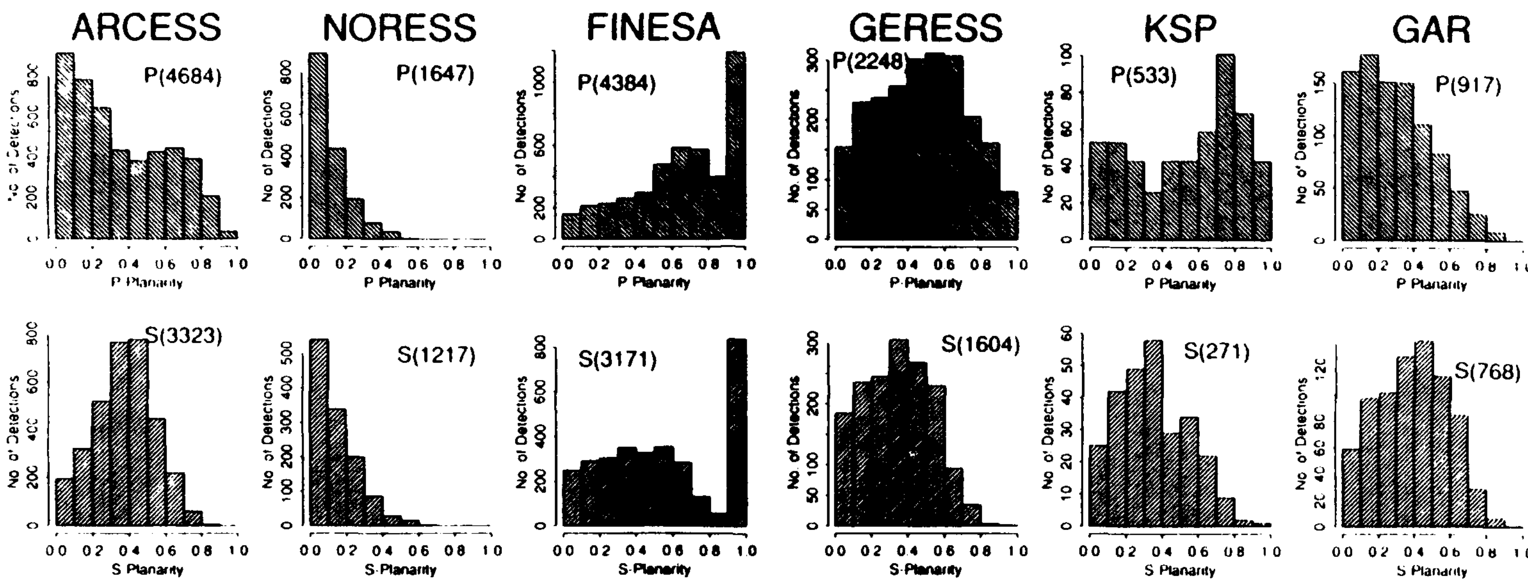

Figure 7. *Histograms of "planarity" are shown for P-type phases (upper) and S-type phases (lower). The numbers in parentheses indicate the number of associated phases. The P and S populations show overlaps at all observing stations.*

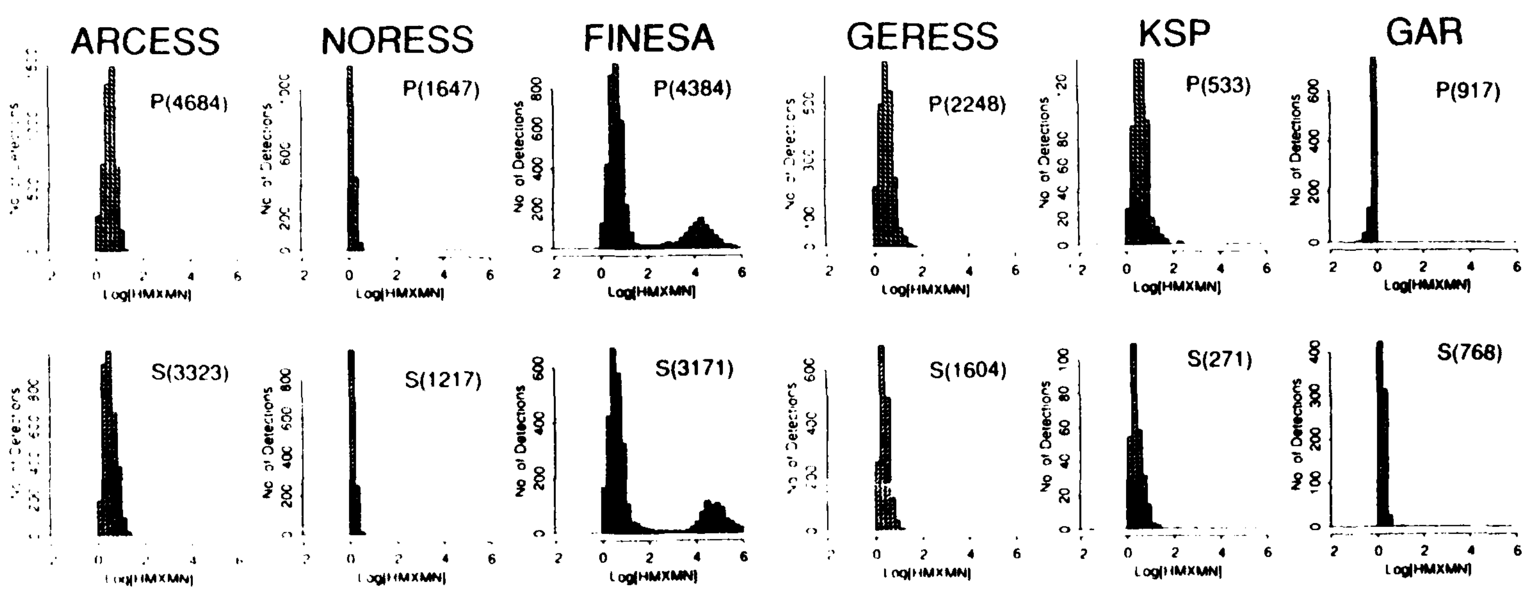

Figure 8. *Histograms of "logarithm of the ratio of maximum to minimum horizontal amplitude" are shown for P-type phases (upper) and S-type phases (lower). The numbers in parentheses indicate the number of associated phases. The P and S populations show overlaps at all observing stations. Although used in IMS as associated detections for event formation, some large values [2<log(HMxMN)<6] of this parameter observed at FINESA are noise detections. These were included in our dataset, as these occurrences may be expected in automated operational situations.*

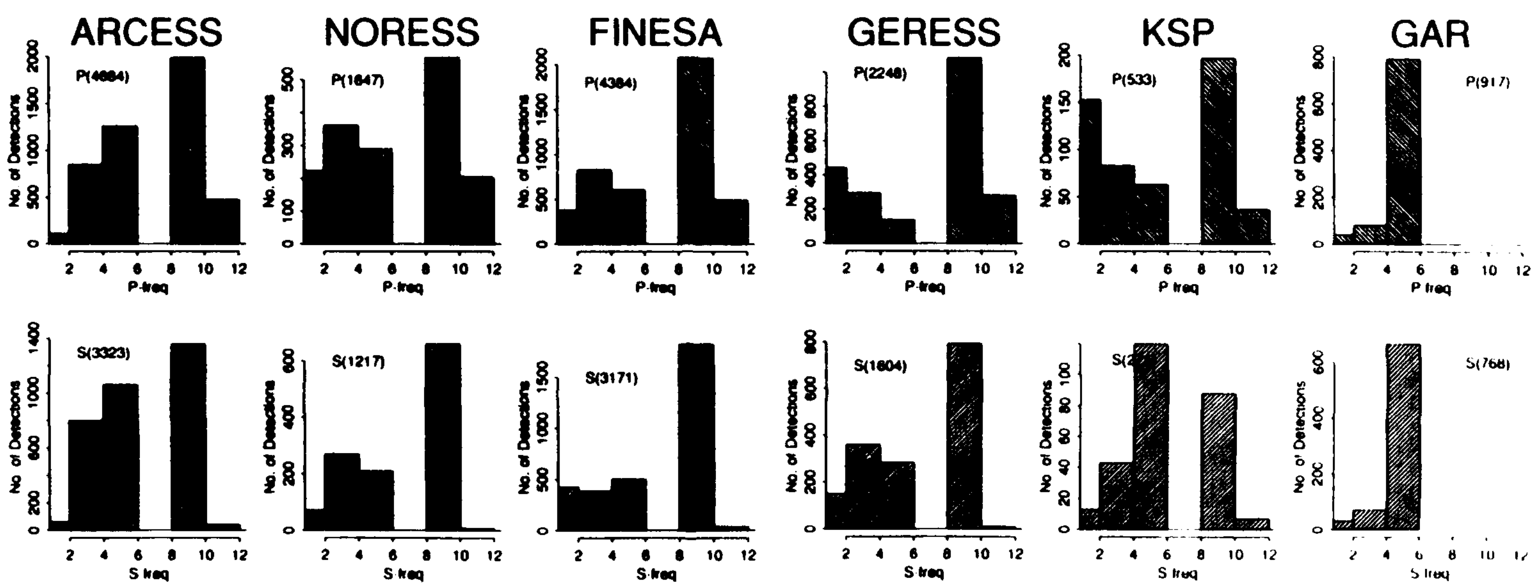

Figure 9. *Histograms of "center frequency of the passbands" are shown for P-type phases (upper) and S-type phases (lower). The numbers in parentheses indicate the number of associated phases. The P and S populations show overlaps at all observing stations.*

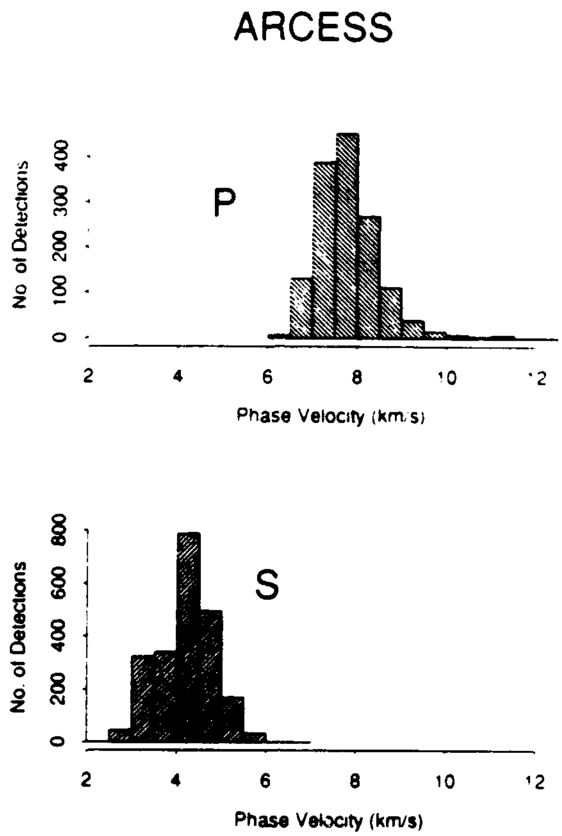

Figure 10. *Phase velocity is plotted for P and S phases recorded at ARCESS. Phase velocity is estimated using a wide-band frequency-wavenumber (f-k) algorithm [Kvaerna and Doornbos, 1986]. This calculation is done using all available vertical channels (up to 25 array elements). Note that a phase velocity of 6 km/s almost perfectly separates P-type and S-type phases.*

3. NEURAL NETWORK SIMULATION

In this section we describe the design and implementation of our neural networks for automated initial identification of seismic phases recorded by 3-component stations. The goal is to identify the phase type (*P* or *S*) based on the polarization attributes described in the previous section.

3.1 Why Neural Networks?

There are several techniques that can be used for automated initial identification of seismic phases using polarization attributes. The current rule-based system of IMS has explicit rules (knowledge sources) for this task. However, it is difficult to develop rules for tasks that use multivariate data (8-10 polarization attributes). In addition, polarization characteristics are site-specific, so a new set of rules must be developed each time a new station is added to the seismic network. Multivariate statistical techniques are applicable in this situation [*Suteau-Henson*, 1991]. However, the required assumption of normality of the data and a linear method renders it sensitive to outliers and noise, particularly for low *snr*. The neural networks used in our study do not require the normality assumption and are less sensitive to outliers. These networks offer a data-intensive, case-based approach to the problem. The functional relation between the polarization attributes and the corresponding phase-type is derived as a network of nodes and weights connecting these nodes. Also, neural networks are amenable to machine-learning techniques and are easily adapted to data from new stations.

There have been successful applications of this technique in seismological problems [*Patnaik,* 1989; *Patnaik, et. al.*, 1990; *Patnaik and Mitchell,* 1990; *Dysart and Pulli,* 1990; and *Dowla, et. al.*, 1990]. In the next section we briefly describe the particular type of neural network used in our study.

3.2 Neural Networks with Back Propagation Training

The neural network architecture that we used has three layers: eight input nodes, four middle (hidden) nodes, and two output nodes (Figure 11). The input layer with eight nodes corresponds to the eight polarization attributes, and two output nodes correspond to *P*-type and *S*-type phases. All of the networks have four middle-layer nodes. The number of these nodes was determined empirically as described in Section 3.3.2. The inputs to each node in the middle layer are weighted sums of the polarization attributes, and the output of a node is calculated by applying a non-linear thresholding function to its input (Figure 12). These nodes act as thresholding units; the thresholding function suppresses the outputs to between 0 and 1. Determination of the appropriate weights among the nodes constitutes network training or learning. The weights w_{ij} converging to a node a_j may be thought of as the coefficients of an equation representing an $[i\text{-}1]$-dimensional plane. Each of the nodes a_j, with their weight w_{ij}, thus partition the input space (training samples) into segments bounded by hyper-planes. These segmented regions each represent a class (sub-class) of the data. During training the positions of these hyper-planes change. The training is based on applications to signals with known output classifications. For network training, we employ a variation of the back-error propagation algorithm described by *Rumelhart and McClelland* [1986].

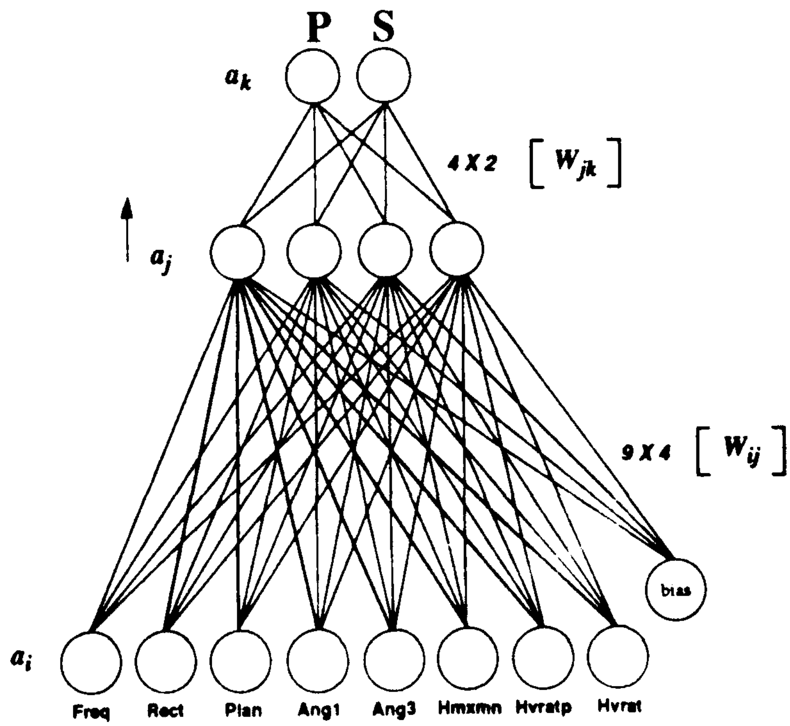

Figure 11. *A simple 3-layer, feed-forward neural network with eight input nodes (a_i), four middle (hidden) nodes (a_j), and two output nodes (a_k). W_{ij} are the weights from input to middle layer and W_{jk} are the weights from middle to output layer.*

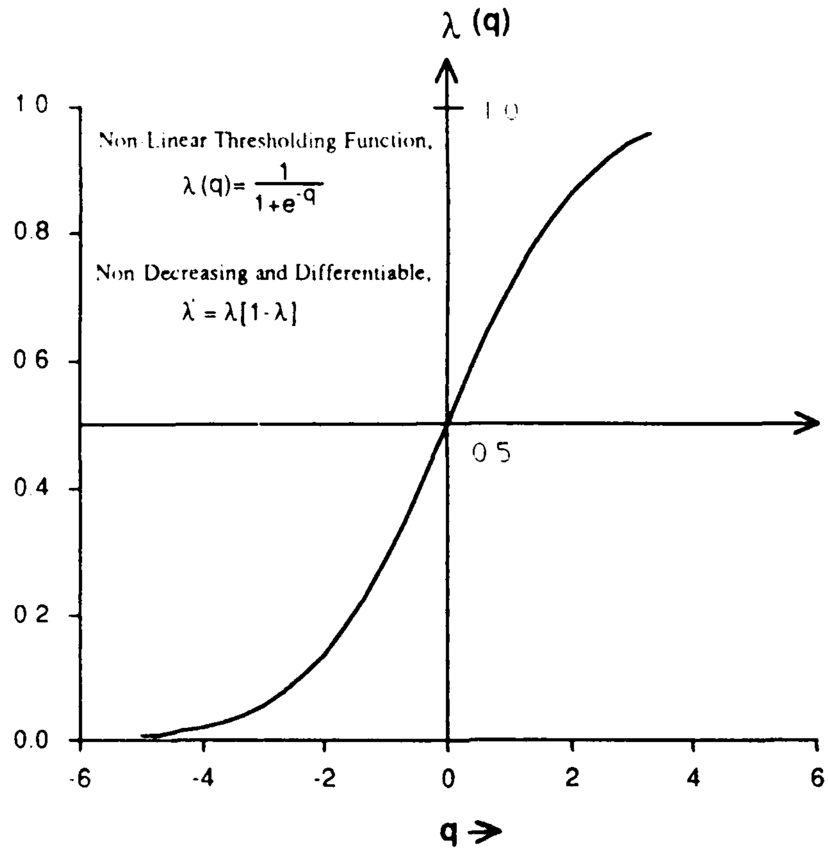

Figure 12. *Non-linear thresholding function used at the middle and output layer nodes.*

The training is accomplished by minimizing the sum square error, E, measured at the output units. This error is

defined as:

$$E = \sum_k (o_k - t_k)^2$$

where o_k is the output produced at node "k" by propagating input patterns $[a_i]$ through the network. The term t_k is the desired output of node "k", which is the teaching signal. The vector $[a_i]$ is the vector of polarization parameters and t_k is either 1 or 0 depending on whether $[a_i]$ corresponds to a *P*-type or *S*-type phase.

An output o_j can be represented as:

$$o_j = \frac{1}{1 + e^{-\sum_i w_{ij} a_i + x_j}}$$

The error term is propagated back to the middle layer nodes using the *generalized delta rule* [*Rumelhart and McClelland,* 1986] which applies weight optimization by the *gradient descent method.* Two parameters called *learning rate* and *momentum constant* that are used in this algorithm are adjusted by trial and error during training. This process was found to be much slower than a conjugate-gradient optimization technique, which we have used for all of our network training. The latter technique also obviates the need for the earlier mentioned heuristic parameters and is much faster.

The term x_j, shown in the expression for a node output, represents a *bias* node. As shown in Figure 11, this bias node produces four weights connecting to the four middle layer nodes. These weights offer *translation* to the dynamics of a network. What it means for a trained network application is that a *bias*, which is dependent on site-specific observed polarization patterns and the number of occurrences of such patterns, is built into the network weights.

3.3 The Method

As described in the previous sections, we use neural networks as pattern matchers. For our purpose, the vector of polarization parameters constitutes a pattern corresponding to a given phase. The ground-truths are analyst-verified phase identifications and are given as teaching inputs. The neural network parameters are problem-dependent (like the number of nodes in the middle layer) and were estimated empirically as described later in this section.

3.3.1 Data Processing

As mentioned in Section 2, the input data for our neural network training were derived from the polarization processing of IMS. The eight polarization attributes described in Section 2 were selected for the available associated *P*-type and *S*-type phases recorded at each station. For these measured attributes, the value of *freq* ranges from 1 Hz to 12 Hz; the incidence angles *inang1* and *inang3* range between 0° and 90°; *rect* and *plans* range between 0.0 and 1.0; and the amplitude and power ratio parameters *hmxmn*, *hvratp* and *hvrat* range from 0 to approximately 10. In order to keep the weights and weight changes small, the usual convention is to scale the input parameters to small numeric values, near ±1. We tried several preprocessing strategies to achieve this. The best performance was obtained by replacing *freq* with *1/freq*, dividing *inang1* and *inang3* by 90, and compressing the amplitude parameters by taking their natural logarithm. Therefore, we applied this preprocessing strategy to the inputs for all of our neural networks.

3.3.2 Architecture

We conducted numerous experiments to choose the optimum network parameters. These experiments involved adjusting the network learning rate, the number of nodes in the middle layer, and the choice of polarization attributes using the 3-component data recorded at ARCESS. For example, our method for selecting the number of nodes in the middle layer is illustrated in Figure 13. This shows the percentage of identification accuracy versus the number of nodes for *P*-type and *S*-type phases recorded at ARCESS. As shown in Figure 13, networks with more than 4-5 nodes in the middle layer increase complexity without improving identification accuracy. Therefore, we implemented four middle layer nodes in all of our networks. Similarly, several combinations of polarization attributes were used as input patterns in order to identify the most significant attributes (e.g., varying number of input nodes). The identification accuracy is close to 85% for all *snr* ARCESS data using four parameters (*rect*, *inang1*, *hvrat* and *inang3*). By adding the rest of the polarization attributes, this accuracy increased by 5-7% without increasing the training time significantly. Therefore, we used all eight polarization attributes as input to our simulations.

EMPIRICALLY ESTIMATED MIDDLE-LAYER NODES

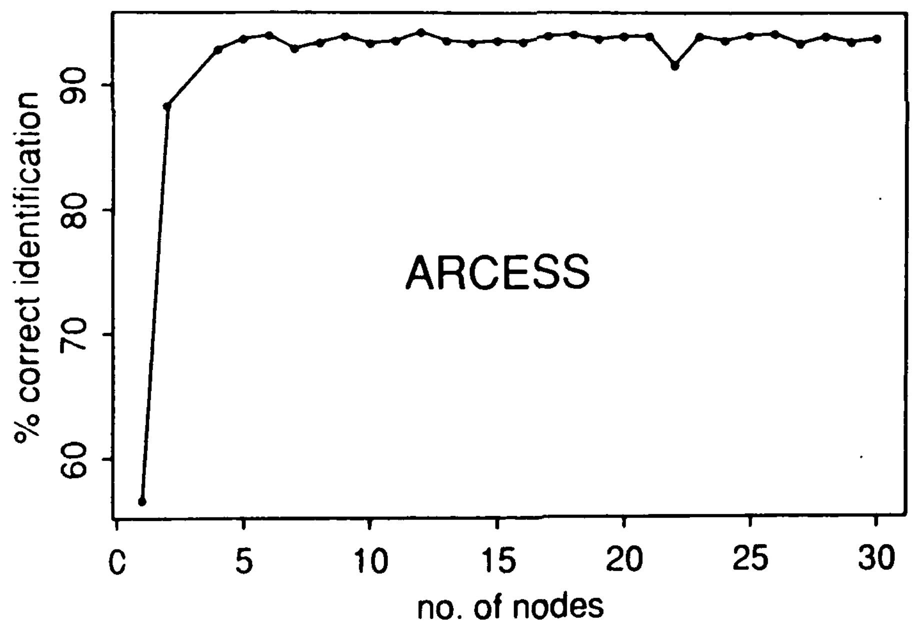

Figure 13. *Percentage identification accuracy versus the number of nodes in the middle layer. This example is for P-type and S-type phases with snr > 2.0 recorded at ARCESS. The networks are of the form 8-X-2, where 8 is the number of inputs, X is the variable number of nodes in the middle layer, and 2 is the number of output nodes (P or S).*

Figure 14 shows the schematic 3-layer architecture for the resulting network for the station GARM. The final weight configurations (two weight matrices) are derived by using the method described in Section 3.2. As shown in Figure 14, the higher activation of the P-output node implies that the set of polarization attributes identified the associated phase as a P-type phase. A node activation value of 0.5 would represent an indeterminate case (see Section 3.3.4).

3.3.3 Network Training

Our results of identification accuracy are based on training the networks with 2/3 of the data, and evaluating the performance (testing) on the remaining 1/3. Stability is established by applying this test three times, each time using a different 1/3 of the data for testing for each station. The results are reported as the average of the three tests, since no appreciable differences among the results for different test sets were noticed.

Training a typical neural network required approximately 500 presentations (forward propagation, backward propagation and weight adjustment) of about 2,000 sample patterns and took less than one hour on a SUN-4 Sparc station. Of course, the training time varies with the sample size when all other network parameters remain the same.

SCHEMATIC 3-LAYER "TRAINED" NETWORK

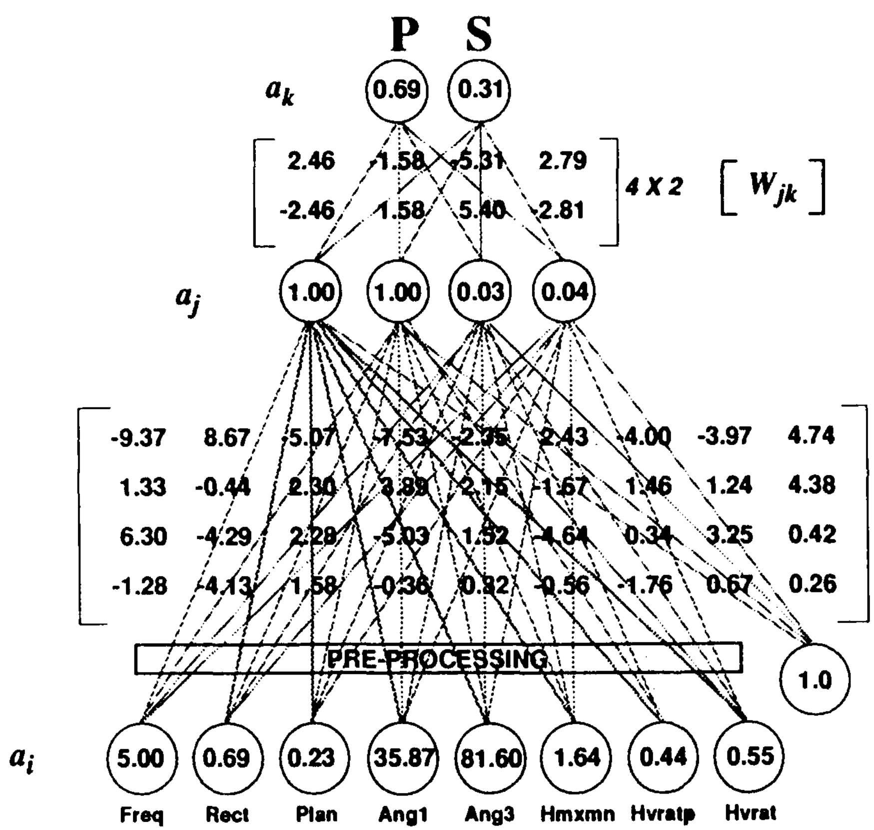

$$p_j = \sum_i w_{ij} a_i + X_j$$

$$a_j = \lambda(p_j)$$

$$\lambda(q) = \frac{1}{1+e^{-q}}$$

Figure 14. *Schematic diagram of a trained, 3-layer, feed-forward, neural network (8-4-2). The input nodes are a_i (polarization attributes); w_{ij} are the weights from input to middle (hidden) layer; a_j are the middle layer nodes; w_{jk} are the weights from middle to output layer; and a_k are the output nodes (P or S). This particular example shows the identification of a P-type phase at GARM.*

3.3.4 Confidence Factors

We estimated an empirical confidence measure for the phase identifications determined by the neural networks (Figure 15) by comparing the output activations of each node to the true phase (ground-truth). As shown in Figure 15, an output activation higher than 0.65 corresponds to greater than 90% confidence in the neural network phase identification for both phases at ARCESS and for *S*-type phases at NORESS. The lower confidence obtained for *P*-type phases at NORESS is perhaps explained by the scattering effect introduced by the heterogeneities beneath the array, causing polarization parameters to be more irregular. This is also noticeable from the histogram distribution, as shown in Figure 2. There are more rigorous methods of the estimation of probability of a phase identification from the outputs of the neural networks, but we have not implemented them in the current version.

EMPIRICALLY-ESTIMATED CONFIDENCE FACTORS

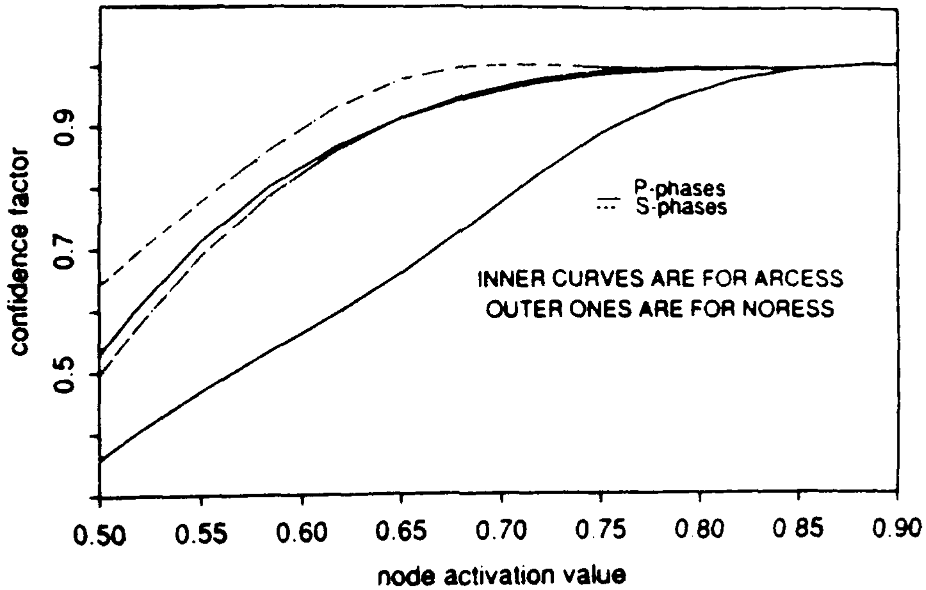

Figure 15. *Empirically-estimated confidence factors for ARCESS (two inner curves) and similarly for NORESS. The solid curves are for P-type phases and the dashed curves are for S-type phases.*

4. RESULTS

The percentage of correct identification for ARCESS and NORESS was 92-99% for data with 3-component *snr* > 2.0 and 86-96% for all *snr*. However, this includes the reduction in variance caused by averaging the four 3-component elements in these arrays. The percentage of correct identification for each individual 3-component station in these arrays is somewhat lower, as described in the next section.

4.1 Single 3-Component Elements of NORESS and ARCESS

To examine the effect of array averaging, which reduces variance in the polarization measurements, we conducted similar network simulations with data from each of the 3-component elements of the arrays ARCESS and NORESS. The results are shown in Table 1. These results show that there are small variations in identification accuracy among data from the individual elements. However, there is about an 8% difference between the results for all *snr* and for *snr* > 2.0.

TABLE 1. SINGLE 3-COMPONENT SITES OF ARRAYS

Average Percentages of Correct Identification of Both *P*-type and *S*-type Phases

ARCESS	ARA0	ARC2	ARC4	ARC7
ALL SNR	85.2	83.3	81.0	81.3
SNR >2	92.4	92.0	87.7	89.5

NORESS	NRA0	NRC2	NRC4	NRC7
ALL SNR	80.5	76.4	79.3	79.8
SNR >2	92.3	89.8	92.4	90.1

4.2 Comparative Evaluation

Another objective of the DARPA neural network program is to evaluate the performance of this technique compared to existing techniques. We compared the neural network results obtained for ARCESS and NORESS data to those obtained using a multivariate discriminant approach on a common data set. The multivariate analysis is being performed by Drs. Anne Suteau-Henson and Jerry Carter at CSS. Preliminary results show that the identification accuracy obtained by neural networks is 3-7% higher than those obtained by the multivariate statistical approach (Table 2). There are some discrepancies in the data set that was used, which may reduce this difference. Nevertheless, the improvements obtained by the neural networks were greater for *S*-type phases than they were for *P*-type phases. We are currently examining the attributes of the phases that were not correctly identified by either method to see if there are consistencies among them that could be used to improve the overall performance.

TABLE 2. COMPARATIVE PERFORMANCE

Percentages of Correct Identification

	ARCESS		ARCESS (SNR > 2)		NORESS		NORESS (SNR > 2)	
	P	S	P	S	P	S	P	S
Neural Network	88.8	95.5	92.5	98.5	86.0	96.0	94.0	99.0
*Multi-variate Discriminant Analysis	86.5	88.5	90.7	92.6	86.2	89.3	94.0	96.0

*[Performed by A. Henson and J. Carter]

4.3 Adaptability

One of the goals of this program is to examine the adaptability (and generality) of the trained neural networks to data from differing geologic environments. We initially tested the generalization capability of trained neural networks and their adaptability to data from a new site by applying them to data recorded by one of the IRIS stations (GARM) in the former Soviet Union. We found that networks that were trained with NORESS/ARCESS data performed at about 80% accuracy level when tested directly with data recorded by GARM, without retraining. The identification accuracy increased by about 10% after retraining, using data recorded at GARM.

Similar experiments were conducted for all the available stations in order to introduce greater variability in the geologic conditions of our tests. Table 3 shows the results of these tests. The polarization data used for these tests have 3-component *snr* >

2.0. In order to have a comparable estimate, we chose data from only one 3-component element of the arrays, ARCESS and NORESS. As shown in Table 3, the diagonals show the training and testing with data from the same station. The off-diagonals show the results of cross-testing (i.e., adaptability testing). It is observed that the identification accuracy is about 10-15% higher if testing and training use data from the same station. A trained network generally shows about 80% correct identification of phases if applied to data from a new site. Thus, the propagation characteristics are similar for all geological environments tested, to the extent that 80% of the detections have similar polarization characteristics. The rest of the increase by 10-15% upon retraining may be attributed to the site-specific characteristics of the different regions.

TABLE 3. ADAPTABILITY

Average Percentages of Correct Identification of Both *P*-type and *S*-type Phases (*snr* > 2)

Train \ Test	ARCESS	NORESS	FINESA	GERESS	KSP	GARM
ARCESS	92.35	87.69	82.11	89.71	77.74	89.09
NORESS	90.69	92.73	76.69	85.75	79.12	80.53
FINESA	89.80	84.27	93.76	86.69	87.20	87.10
GERESS	90.36	87.27	83.17	91.06	77.05	88.31
KSP	83.80	84.97	81.81	78.77	92.39	80.71
GARM	59.33	68.60	72.22	80.54	70.24	93.43

4.4 Adding Context

The polarization attributes that were used for neural network phase identification did not have any contextual information, such as the information about relative detection time of the corresponding phases. Therefore, as a next step we augmented the polarization data with "context" in an effort to improve identification accuracy. So far we have considered two such contexts. One of these is the difference between the number of detections that arrive before the detection in question and the number of detections following it for a fixed time window. An example of the distribution of this parameter is shown in Figure 16 for the arrivals at the station KSP. The figure also shows another contextual parameter obtained from the mean time differences between the detection in question and detections before and after it within a fixed time window. These contextual parameters show better separations than many of the polarization attributes (Figures 2 - 9). When these are added to the polarization parameters in separate simulations, the percentage of correct identification of phases observed at KSP increased by 3-5%. The window length used in the contextual parameter was chosen empirically, and is governed by the nature of the seismicity observed at a given station.

CONTEXTUAL PARAMETERS (30 SECOND WINDOW)

KSP

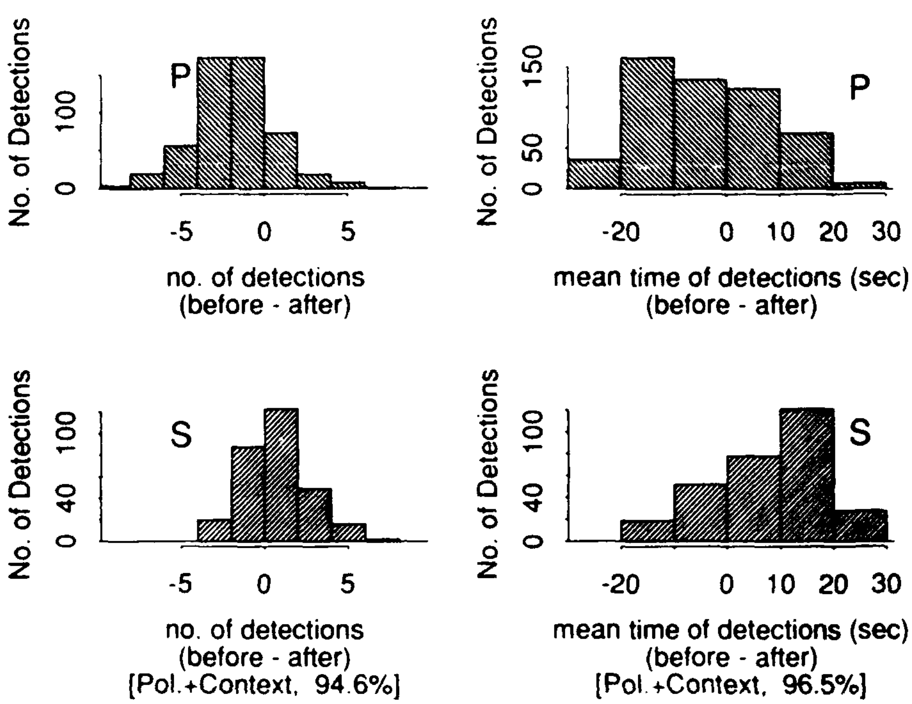

Figure 16. *The histograms on the left show the difference between the number of detections that arrive before the detection in question and the number of detections following it, for a fixed window length of 30 seconds. Similarly, the histograms on the right show the differences between the mean arrival times before and after the detection in question within a fixed time window.*

5. INTEGRATION INTO IMS

We are currently replacing the rule-based initial phase identification in IMS with our neural network approach. We have implemented the neural network module for initial phase identification into a test version of ESAL, which is a knowledge-based system component of IMS. This initial implementation will allow us to choose between the neural network and the rule-based methods so that we can apply both to the same data (Figure 17). This will provide a basis for a direct comparison of the two methods under operational conditions. We will test this performance using 3-component data recorded by the IRIS stations in the former Soviet Union.

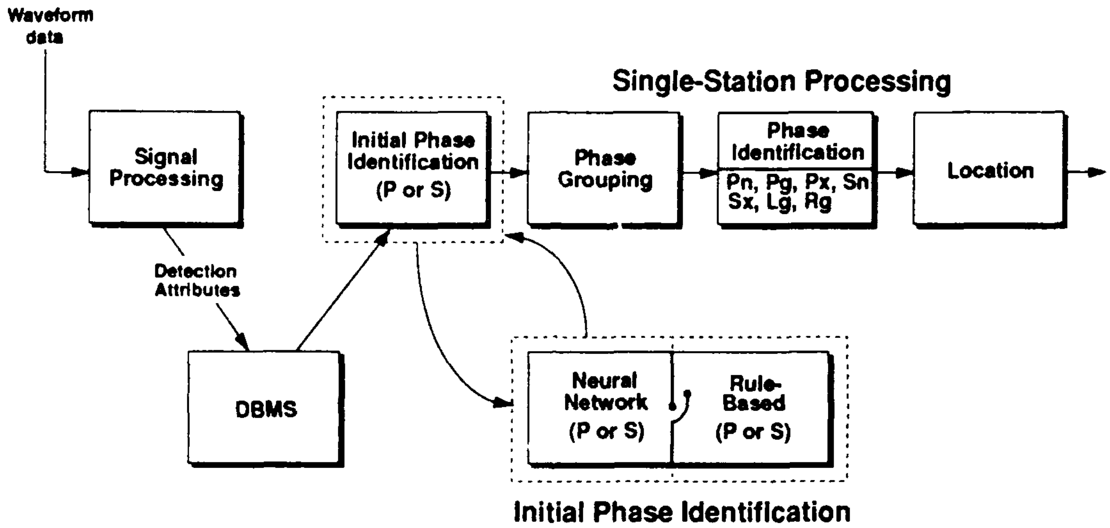

Figure17. System Integration. *This diagram shows the integration of the neural network initial phase identification module into the rule-based component (Expert System for Association and Location) of the IMS system. The initial phase identification element of the expert system will be replaced by a trained neural network.*

6. SUMMARY

We have developed and implemented a neural network technique for initial phase identification using polarization measurements from 3-component data. This technique has the following advantages:

- It is easier to develop than rules because phase identification is based on high-dimensional multivariate input data.
- It incorporates station-specific characteristics.
- It performs 3-7% better than a linear multivariate discriminant analysis method (particularly for data with low *snr*).
- It is easily adapted to data from new stations. For example, we find that we achieve 75-80% identification accuracy for a new station without system retraining (e.g., using a network derived from data from a different station). The data required for retraining can be accumulated in about two weeks of continuous operation of the new station, and training takes less than one hour on a Sun4 Sparc station. After this retraining, the identification accuracy increases to > 90%.

These neural networks are being implemented into DARPA's Intelligent Monitoring System which is in operation at the Center for Seismic Studies.

ACKNOWLEDGEMENTS

We thank Drs. Anne Suteau-Henson and Jerry Carter for their collaboration in the comparative evaluation of the neural network results. Florence Riviere-Barbier kindly provided the processed IRIS data used in this study. We acknowledge Richard Jenkin's help in our system integration effort. We would also like to thank our colleagues at SAIC and at the Center for Seismic Studies for their help and discussions throughout this work. Christine Ferraro edited and prepared this document. This research was supported by the Defense Advanced Research Projects Agency under Contract #F19628-90-C-0156 and monitored by Phillips Laboratory, Hanscom AFB.

REFERENCES

Bache, T., S. Bratt, J. Wang, R. Fung, C. Kobryn, and J. Given, "The Intelligent Monitoring System", *Bull. Seism. Soc. Am.*, **80**, Part B, p.1833-1851, 1990.

Dowla, F., S. Taylor, and R. Anderson, Seismic Discrimination with Artificial Neural Networks: Preliminary Results with Regional Spectral Data, *Bull. Seism. Soc.* Am., **80**, 1346-1373, 1990.

Dysart, P., and J. Pulli, "Regional Seismic Event Classification at the NORESS Array: Seismological Measurements and the Use of Trained Neural Networks", *Bull. Seism. Soc. Am.*, **80**, Part B, p.1910-1933, 1990.

Jurkevics, A., "Polarization Analysis of 3-Component Array Data", *Bull. Seism. Soc. Am.*, **78**, p.1725-1743, 1988.

Kvaerna, T. and D.J. Doornbos, "An Integrated Approach to Slowness Analysis with Arrays and 3-Component Stations, *Semi-annual Technical Summary,* 10/1/85-3/31/86, NORSAR Scientific Report No. 2- 85/86, Kjeller, Norway, 1986.

Patnaik, G.B., "Seismic Surface Wave Type Classification Using Artificial Neural Networks, *GSA Abstracts with Programs*, Vol. 21, No. 6, p. A256, 1989.

Patnaik, G.B., B.J. Mitchell, and G.V. Rao, "Learned Classification of Seismic Events on Massively Parallel Networks", *Paper presented at the Annual Meeting of the Missouri Academy of Sciences, St. Louis, Missouri*, 28 April 1990.

Patnaik, G.B., and B.J. Mitchell, "Focal Depth Estimation with Multilayered Neural Networks", Proceedings of the Twelfth Annual DARPA/GL Seismic Research Symposium, *GL-TR-90-0212*, Special Reports, **261**, p.320-326, 18-20 September 1990. **ADA226635**

Rumelhart, D.E., J.L. McClelland, and the PDP Group, "Parallel Distributed Processing, Explorations in the Microstructure of Cognition", *MIT Press*, **1**, p.547, 1986.

Sereno, T., and G. Patnaik, "Data to Test and Evaluate the Performance of Neural Network Architectures for Seismic Signal Discrimination--DARPA Data Set #1", *Annual Technical Report* (Vol. I), SAIC-91/1236, Science Applications International Corporation, San Diego, California, 1991.

Suteau-Henson, A., "3-Component Analysis of Regional Phases at NORESS and ARCESS: Polarization and Phase Identification", in Nuclear Monitoring Research at the Center for Seismic Studies, Scientific Report No. 1, *PL-TR-91-2127*, p.2-1 through 2-32, 13 May 1991, ADA239653.

DISTRIBUTION LIST

Prof. Thomas Ahrens
Seismological Lab, 252-21
Division of Geological & Planetary Sciences
California Institute of Technology
Pasadena, CA 91125

Prof. Keiiti Aki
Center for Earth Sciences
University of Southern California
University Park
Los Angeles, CA 90089-0741

Prof. Shelton Alexander
Geosciences Department
403 Deike Building
The Pennsylvania State University
University Park, PA 16802

Dr. Ralph Alewine, III
DARPA/NMRO
3701 North Fairfax Drive
Arlington, VA 22203-1714

Prof. Charles B. Archambeau
CIRES
University of Colorado
Boulder, CO 80309

Dr. Thomas C. Bache, Jr.
Science Applications Int'l Corp.
10260 Campus Point Drive
San Diego, CA 92121 (2 copies)

Prof. Muawia Barazangi
Institute for the Study of the Continent
Cornell University
Ithaca, NY 14853

Dr. Jeff Barker
Department of Geological Sciences
State University of New York
at Binghamton
Vestal, NY 13901

Dr. Douglas R. Baumgardt
ENSCO, Inc
5400 Port Royal Road
Springfield, VA 22151-2388

Dr. Susan Beck
Department of Geosciences
Building #77
University of Arizona
Tuscon, AZ 85721

Dr. T.J. Bennett
S-CUBED
A Division of Maxwell Laboratories
11800 Sunrise Valley Drive, Suite 1212
Reston, VA 22091

Dr. Robert Blandford
AFTAC/TT, Center for Seismic Studies
1300 North 17th Street
Suite 1450
Arlington, VA 22209-2308

Dr. G.A. Bollinger
Department of Geological Sciences
Virginia Polytechnical Institute
21044 Derring Hall
Blacksburg, VA 24061

Dr. Stephen Bratt
Center for Seismic Studies
1300 North 17th Street
Suite 1450
Arlington, VA 22209-2308

Dr. Lawrence Burdick
Woodward-Clyde Consultants
566 El Dorado Street
Pasadena, CA 91109-3245

Dr. Robert Burridge
Schlumberger-Doll Research Center
Old Quarry Road
Ridgefield, CT 06877

Dr. Jerry Carter
Center for Seismic Studies
1300 North 17th Street
Suite 1450
Arlington, VA 22209-2308

Dr. Eric Chael
Division 9241
Sandia Laboratory
Albuquerque, NM 87185

Prof. Vernon F. Cormier
Department of Geology & Geophysics
U-45, Room 207
University of Connecticut
Storrs, CT 06268

Prof. Steven Day
Department of Geological Sciences
San Diego State University
San Diego, CA 92182

Marvin Denny
U.S. Department of Energy
Office of Arms Control
Washington, DC 20585

Dr. Zoltan Der
ENSCO, Inc.
5400 Port Royal Road
Springfield, VA 22151-2388

Prof. Adam Dziewonski
Hoffman Laboratory, Harvard University
Dept. of Earth Atmos. & Planetary Sciences
20 Oxford Street
Cambridge, MA 02138

Prof. John Ebel
Department of Geology & Geophysics
Boston College
Chestnut Hill, MA 02167

Eric Fielding
SNEE Hall
INSTOC
Cornell University
Ithaca, NY 14853

Dr. Mark D. Fisk
Mission Research Corporation
735 State Street
P.O. Drawer 719
Santa Barbara, CA 93102

Prof Stanley Flatte
Applied Sciences Building
University of California, Santa Cruz
Santa Cruz, CA 95064

Dr. John Foley
NER-Geo Sciences
1100 Crown Colony Drive
Quincy, MA 02169

Prof. Donald Forsyth
Department of Geological Sciences
Brown University
Providence, RI 02912

Dr. Art Frankel
U.S. Geological Survey
922 National Center
Reston, VA 22092

Dr. Cliff Frolich
Institute of Geophysics
8701 North Mopac
Austin, TX 78759

Dr. Holly Given
IGPP, A-025
Scripps Institute of Oceanography
University of California, San Diego
La Jolla, CA 92093

Dr. Jeffrey W. Given
SAIC
10260 Campus Point Drive
San Diego, CA 92121

Dr. Dale Glover
Defense Intelligence Agency
ATTN: ODT-1B
Washington, DC 20301

Dr. Indra Gupta
Teledyne Geotech
314 Montgomery Street
Alexanderia, VA 22314

Dan N. Hagedon
Pacific Northwest Laboratories
Battelle Boulevard
Richland, WA 99352

Dr. James Hannon
Lawrence Livermore National Laboratory
P.O. Box 808
L-205
Livermore, CA 94550

Dr. Roger Hansen
HQ AFTAC/TTR
Patrick AFB, FL 32925-6001

Prof. David G. Harkrider
Seismological Laboratory
Division of Geological & Planetary Sciences
California Institute of Technology
Pasadena, CA 91125

Prof. Danny Harvey
CIRES
University of Colorado
Boulder, CO 80309

Prof. Donald V. Helmberger
Seismological Laboratory
Division of Geological & Planetary Sciences
California Institute of Technology
Pasadena, CA 91125

Prof. Eugene Herrin
Institute for the Study of Earth and Man
Geophysical Laboratory
Southern Methodist University
Dallas TX 75275

Prof. Robert B. Herrmann
Department of Earth & Atmospheric Sciences
St. Louis University
St. Louis, MO 63156

Prof. Lane R. Johnson
Seismographic Station
University of California
Berkeley, CA 94720

Prof. Thomas H. Jordan
Department of Earth, Atmospheric &
Planetary Sciences
Massachusetts Institute of Technology
Cambridge, MA 02139

Prof. Alan Kafka
Department of Geology & Geophysics
Boston College
Chestnut Hill, MA 02167

Robert C. Kemerait
ENSCO, Inc.
445 Pineda Court
Melbourne, FL 32940

Dr. Max Koontz
U.S. Dept. of Energy/DP 5
Forrestal Building
1000 Independence Avenue
Washington, DC 20585

Dr. Richard LaCoss
MIT Lincoln Laboratory, M-200B
P.O. Box 73
Lexington, MA 02173-0073

Dr. Fred K. Lamb
University of Illinois at Urbana-Champaign
Department of Physics
1110 West Green Street
Urbana, IL 61801

Prof. Charles A. Langston
Geosciences Department
403 Deike Building
The Pennsylvania State University
University Park, PA 16802

Jim Lawson, Chief Geophysicist
Oklahoma Geological Survey
Oklahoma Geophysical Observatory
P.O. Box 8
Leonard, OK 74043-0008

Prof. Thorne Lay
Institute of Tectonics
Earth Science Board
University of California, Santa Cruz
Santa Cruz, CA 95064

Dr. William Leith
U.S. Geological Survey
Mail Stop 928
Reston, VA 22092

Mr. James F. Lewkowicz
Phillips Laboratory/GPEH
Hanscom AFB, MA 01731-5000(2 copies)

Mr. Alfred Lieberman
ACDA/VI-OA State Department Building
Room 5726
320-21st Street, NW
Washington, DC 20451

Prof. L. Timothy Long
School of Geophysical Sciences
Georgia Institute of Technology
Atlanta, GA 30332

Dr. Randolph Martin, III
New England Research, Inc.
76 Olcott Drive
White River Junction, VT 05001

Dr. Robert Masse
Denver Federal Building
Box 25046, Mail Stop 967
Denver, CO 80225

Dr. Gary McCartor
Department of Physics
Southern Methodist University
Dallas, TX 75275

Prof. Thomas V. McEvilly
Seismographic Station
University of California
Berkeley, CA 94720

Dr. Art McGarr
U.S. Geological Survey
Mail Stop 977
U.S. Geological Survey
Menlo Park, CA 94025

Dr. Keith L. McLaughlin
S-CUBED
A Division of Maxwell Laboratory
P.O. Box 1620
La Jolla, CA 92038-1620

Stephen Miller & Dr. Alexander Florence
SRI International
333 Ravenswood Avenue
Box AF 116
Menlo Park, CA 94025-3493

Prof. Bernard Minster
IGPP, A-025
Scripps Institute of Oceanography
University of California, San Diego
La Jolla, CA 92093

Prof. Brian J. Mitchell
Department of Earth & Atmospheric Sciences
St. Louis University
St. Louis, MO 63156

Mr. Jack Murphy
S-CUBED
A Division of Maxwell Laboratory
11800 Sunrise Valley Drive, Suite 1212
Reston, VA 22091 (2 Copies)

Dr. Keith K. Nakanishi
Lawrence Livermore National Laboratory
L-025
P.O. Box 808
Livermore, CA 94550

Dr. Carl Newton
Los Alamos National Laboratory
P.O. Box 1663
Mail Stop C335, Group ESS-3
Los Alamos, NM 87545

Dr. Bao Nguyen
HQ AFTAC/TTR
Patrick AFB, FL 32925-6001

Prof. John A. Orcutt
IGPP, A-025
Scripps Institute of Oceanography
University of California, San Diego
La Jolla, CA 92093

Prof. Jeffrey Park
Kline Geology Laboratory
P.O. Box 6666
New Haven, CT 06511-8130

Dr. Howard Patton
Lawrence Livermore National Laboratory
L-025
P.O. Box 808
Livermore, CA 94550

Dr. Frank Pilotte
HQ AFTAC/TT
Patrick AFB, FL 32925-6001

Dr. Jay J. Pulli
Radix Systems, Inc.
2 Taft Court, Suite 203
Rockville, MD 20850

Dr. Robert Reinke
ATTN: FCTVTD
Field Command
Defense Nuclear Agency
Kirtland AFB, NM 87115

Prof. Paul G. Richards
Lamont-Doherty Geological Observatory
of Columbia University
Palisades, NY 10964

Mr. Wilmer Rivers
Teledyne Geotech
314 Montgomery Street
Alexandria, VA 22314

Dr. George Rothe
HQ AFTAC/TTR
Patrick AFB, FL 32925-6001

Dr. Alan S. Ryall, Jr.
DARPA/NMRO
3701 North Fairfax Drive
Arlington, VA 22209-1714

Dr. Richard Sailor
TASC, Inc.
55 Walkers Brook Drive
Reading, MA 01867

Prof. Charles G. Sammis
Center for Earth Sciences
University of Southern California
University Park
Los Angeles, CA 90089-0741

Prof. Christopher H. Scholz
Lamont-Doherty Geological Observatory
of Columbia University
Palisades, CA 10964

Dr. Susan Schwartz
Institute of Tectonics
1156 High Street
Santa Cruz, CA 95064

Secretary of the Air Force
(SAFRD)
Washington, DC 20330

Office of the Secretary of Defense
DDR&E
Washington, DC 20330

Thomas J. Sereno, Jr.
Science Application Int'l Corp.
10260 Campus Point Drive
San Diego, CA 92121

Dr. Michael Shore
Defense Nuclear Agency/SPSS
6801 Telegraph Road
Alexandria, VA 22310

Dr. Matthew Sibol
Virginia Tech
Seismological Observatory
4044 Derring Hall
Blacksburg, VA 24061-0420

Prof. David G. Simpson
IRIS, Inc.
1616 North Fort Myer Drive
Suite 1440
Arlington, VA 22209

Donald L. Springer
Lawrence Livermore National Laboratory
L-025
P.O. Box 808
Livermore, CA 94550

Dr. Jeffrey Stevens
S-CUBED
A Division of Maxwell Laboratory
P.O. Box 1620
La Jolla, CA 92038-1620

Lt. Col. Jim Stobie
ATTN: AFOSR/NL
Bolling AFB
Washington, DC 20332-6448

Prof. Brian Stump
Institute for the Study of Earth & Man
Geophysical Laboratory
Southern Methodist University
Dallas, TX 75275

Prof. Jeremiah Sullivan
University of Illinois at Urbana-Champaign
Department of Physics
1110 West Green Street
Urbana, IL 61801

Prof. L. Sykes
Lamont-Doherty Geological Observatory
of Columbia University
Palisades, NY 10964

Dr. David Taylor
ENSCO, Inc.
445 Pineda Court
Melbourne, FL 32940

Dr. Steven R. Taylor
Los Alamos National Laboratory
P.O. Box 1663
Mail Stop C335
Los Alamos, NM 87545

Prof. Clifford Thurber
University of Wisconsin-Madison
Department of Geology & Geophysics
1215 West Dayton Street
Madison, WS 53706

Prof. M. Nafi Toksoz
Earth Resources Lab
Massachusetts Institute of Technology
42 Carleton Street
Cambridge, MA 02142

Dr. Larry Turnbull
CIA-OSWR/NED
Washington, DC 20505

Dr. Gregory van der Vink
IRIS, Inc.
1616 North Fort Myer Drive
Suite 1440
Arlington, VA 22209

Dr. Karl Veith
EG&G
5211 Auth Road
Suite 240
Suitland, MD 20746

Prof. Terry C. Wallace
Department of Geosciences
Building #77
University of Arizona
Tuscon, AZ 85721

Dr. Thomas Weaver
Los Alamos National Laboratory
P.O. Box 1663
Mail Stop C335
Los Alamos, NM 87545

Dr. William Wortman
Mission Research Corporation
8560 Cinderbed Road
Suite 700
Newington, VA 22122

Prof. Francis T. Wu
Department of Geological Sciences
State University of New York
at Binghamton
Vestal, NY 13901

AFTAC/CA
(STINFO)
Patrick AFB, FL 32925-6001

DARPA/PM
3701 North Fairfax Drive
Arlington, VA 22203-1714

DARPA/RMO/RETRIEVAL
3701 North Fairfax Drive
Arlington, VA 22203-1714

DARPA/RMO/SECURITY OFFICE
3701 North Fairfax Drive
Arlington, VA 22203-1714

HQ DNA
ATTN: Technical Library
Washington, DC 20305

Defense Intelligence Agency
Directorate for Scientific & Technical Intelligence
ATTN: DTIB
Washington, DC 20340-6158

Defense Technical Information Center
Cameron Station
Alexandria, VA 22314 (2 Copies)

TACTEC
Battelle Memorial Institute
505 King Avenue
Columbus, OH 43201 (Final Report)

Phillips Laboratory
ATTN: XPG
Hanscom AFB, MA 01731-5000

Phillips Laboratory
ATTN: GPE
Hanscom AFB, MA 01731-5000

Phillips Laboratory
ATTN: TSML
Hanscom AFB, MA 01731-5000

Phillips Laboratory
ATTN: SUL
Kirtland, NM 87117 (2 copies)

Dr. Michel Bouchon
I.R.I.G.M.-B.P. 68
38402 St. Martin D'Heres
Cedex, FRANCE

Dr. Michel Campillo
Observatoire de Grenoble
I.R.I.G.M.-B.P. 53
38041 Grenoble, FRANCE

Dr. Kin Yip Chun
Geophysics Division
Physics Department
University of Toronto
Ontario, CANADA

Prof. Hans-Peter Harjes
Institute for Geophysic
Ruhr University/Bochum
P.O. Box 102148
4630 Bochum 1, GERMANY

Prof. Eystein Husebye
NTNF/NORSAR
P.O. Box 51
N-2007 Kjeller, NORWAY

David Jepsen
Acting Head, Nuclear Monitoring Section
Bureau of Mineral Resources
Geology and Geophysics
G.P.O. Box 378, Canberra, AUSTRALIA

Ms. Eva Johannisson
Senior Research Officer
National Defense Research Inst.
P.O. Box 27322
S-102 54 Stockholm, SWEDEN

Dr. Peter Marshall
Procurement Executive
Ministry of Defense
Blacknest, Brimpton
Reading FG7-FRS, UNITED KINGDOM

Dr. Bernard Massinon, Dr. Pierre Mechler
Societe Radiomana
27 rue Claude Bernard
75005 Paris, FRANCE (2 Copies)

Dr. Svein Mykkeltveit
NTNT/NORSAR
P.O. Box 51
N-2007 Kjeller, NORWAY (3 Copies)

Prof. Keith Priestley
University of Cambridge
Bullard Labs, Dept. of Earth Sciences
Madingley Rise, Madingley Road
Cambridge CB3 OEZ, ENGLAND

Dr. Jorg Schlittenhardt
Federal Institute for Geosciences & Nat'l Res.
Postfach 510153
D-3000 Hannover 51, GERMANY

Dr. Johannes Schweitzer
Institute of Geophysics
Ruhr University/Bochum
P.O. Box 1102148
4360 Bochum 1, GERMANY

Commander and Director
USAE Waterways Experiment Station
Attn: CEWES-IM-MI-R
Alfrieda S. Clark, CD Dept/0597
3909 Halls Ferry Road
Vicksburg, MS 39180-6199